Article

Enhanced Photocatalytic Performances of SnS$_2$/TiO$_2$ Composites via a Charge Separation Following Z-Scheme at the SnS$_2$/TiO$_2${101} Facets

Nkenku Carl [1] , Muhammad Fiaz [2] , Hyun-Seok Oh [1] and Yu-Kwon Kim [1,2,*]

[1] Department of Energy Systems Research, Ajou University, Suwon 16499, Republic of Korea; nkenkuc@gmail.com (N.C.); jejuohs@ajou.ac.kr (H.-S.O.)
[2] Department of Chemistry, Ajou University, Suwon 16499, Republic of Korea; fiaz@ajou.ac.kr
* Correspondence: yukwonkim@ajou.ac.kr; Tel.: +82-31-219-2896

Abstract: The formation of heterojunctions for efficient charge separation has been practiced for the preparation of efficient semiconductor-based photocatalysts for applications such as hydrogen production and environmental remediation. In this study, we synthesized a composite structure with a heterojunction between SnS$_2$ and TiO$_2$ through a microwave-assisted hydrothermal process, in which SnS$_2$ nanoparticles grew on nanocrystalline TiO$_2$ nanosheets preferentially at the exposed {101} facets. Appropriate exposure of the {001} and {101} facets of the TiO$_2$ nanosheet in the composite with a preferential growth of SnS$_2$ nanoparticles at the {101} facets was the origin of the charge separation following a direct Z-scheme mechanism to result in enhanced photocatalytic performances in photodegradation of organic dyes such as methylene blue (MB) and rhodamine B (RhB) compared to that of SnS$_2$ and TiO$_2$ alone. A plot of photodegradation rates vs. SnS$_2$ ratios in the composites gave an overall volcano-shaped curve with a maximum at the SnS$_2$ ratio of about 33% at which small SnS$_2$ nanoparticles were populated at the {101} facets of the TiO$_2$ nanosheets with a high surface area (118.2 m^{2}g^{-1}). Our results suggest the microwave-assisted hydrothermal process can be a good synthetic approach for composite-based photocatalysts with a preferential heterojunction structure.

Keywords: SnS$_2$ nanoparticles; TiO$_2$ nanosheets; 2D metal dichalcogenides; photodegradation; heterojunctions

1. Introduction

The design of efficient photocatalytic materials can pave the way not only to utilize energy directly from the Sun as a means to meet the growing world's energy demand but also to eliminate harmful organic compounds for environmental remediation through photocatalytic degradation via direct light-induced chemical reactions mediated by photogenerated electrons and holes [1,2]. Organic dyes can be good examples of harmful compounds that can be soluble in water and remain for a long time to affect our ecosystems. Organic dyes are commonly used in various areas of our daily life, such as papers, printing, and textiles, and usually have a high degree of chemical stability [1]. To eliminate such stable but harmful compounds, the use of photocatalysts can ultimately be an environmentally friendly way of accelerating degradation reactions.

Among various photoactive materials, TiO$_2$ is considered a preferred photocatalyst due to its high reduction potential with a sufficiently large band gap, in addition to its nontoxicity, low cost, and high stability [3]. Furthermore, studies based on shape-controlled synthesis of TiO$_2$ have revealed many interesting aspects of the origin of its photoactivity. For example, the photoactivity of anatase TiO$_2$ has been shown to vary depending on the exposed facets, such as {101} and {001} [4]. The ratio of exposed facets has been effectively controlled to observe high photoactivities attributed to {001} [5–7] and {101} facets [8], respectively, despite the advantageous properties of TiO$_2$, the wide band gap of

about 3.2 eV limits light absorption to the UV region (wavelength below 400 nm) and its photocatalytic activity as well.

The photoactivity of TiO_2 can be further enhanced by making use of both the preferential charge separation of TiO_2 and the enhanced absorption by a visible-light-active photocatalyst through a proper heterojunction between them. Forming a heterojunction of the photocatalyst in the preferred facets of TiO_2 can effectively suppress the recombination of photogenerated e^-–h^+ pairs, which can extend the lifetime of the hot carriers on the surface to improve surface reaction efficiencies [9]. Combining TiO_2 with narrow bandgap semiconductors by forming heterojunctions is a successful approach to extend not only the light absorption range but also the charge carrier lifetime via charge separation at the heterojunctions [10]. As a result, enhanced photoactivity has been reported for various types of TiO_2-based composites such as MoS_2/TiO_2 [11], SnO/TiO_2 [12], TiO_2/g-C_3N_4 [10] and CdS/TiO_2 [13].

SnS_2 is a layered transition metal dichalcogenide (TMD) with a narrow band gap (2.18–2.44 eV) that can act as a charge transfer medium as well as active sites for catalytic reactions [14] and is gaining increasing attention as a photocatalyst for solar-driven reactions and degradation of organic pollutants. This is due to its cost-effectiveness, non-toxicity, and unique physicochemical characteristics [15]. However, SnS_2 is also limited by its high recombination rate, which can be mitigated by forming heterojunctions. These heterojunctions enhance the charge separation of photo-excited electron–hole pairs [16].

In this study, we synthesized composites of SnS_2/TiO_2 with the intention of exploring the photodegradation performances of the composites in relation to properties such as charge separation at heterojunctions and enhanced visible light absorption due to SnS_2. As a composite preparation method, we employed a microwave-assisted hydrothermal process, which was found to be a facile hydrothermal method of preparing SnS_2/TiO_2 composites with coupled 2D heterojunctions. The synthesized composites were found to show enhanced photocatalytic activity in the photodegradation of both methylene blue (MB) and rhodamine B (RhB) in an aqueous solution, largely due to enhanced charge separation at the heterojunction via the Z-scheme.

2. Results and Discussion

2.1. Characteristics of SnS₂/TiO₂ Composites

Figure 1 shows the X-ray diffraction (XRD) spectra of the as-synthesized composites compared to those of as-synthesized SnS_2 and TiO_2 as references. The XRD spectrum of the as-synthesized SnS_2 nanoparticles exhibits the characteristics of hexagonal SnS_2 structure (JCPDS no. 01-1010) [17]. Additionally, as-synthesized TiO_2 nanosheets give an XRD spectrum with the characteristic peaks of anatase phase TiO_2 without the presence of a rutile phase (JCPDS card no. 21-1272) [18]. The intense (200) diffraction of anatase TiO_2 compared to (004) originates from the shape of the nanosheets with the large (001) facets of anatase TiO_2 [19,20], which is due to the surfactant-mediated preferential growth mediated by surfactant toward directions perpendicular to (001). The XRD patterns of the SnS_2/TiO_2 composites display the characteristic peaks of the anatase TiO_2 and hexagonal SnS_2 only, indicating the selective formation of both phases in the compounds with varying ratios of SnS_2. The intensity ratios of the peak SnS_2 (001) to the TiO_2 (101) or (004) change in accordance with the mole ratio of SnS_2 to TiO_2 with increasing %SnS_2 content. Figure S1 contains the XRD patterns of all the prepared composites. The results indicate that the microwave process can generate composites based on both the hexagonal SnS_2 and the anatase TiO_2 phases over a wide range of SnS_2 mole ratios.
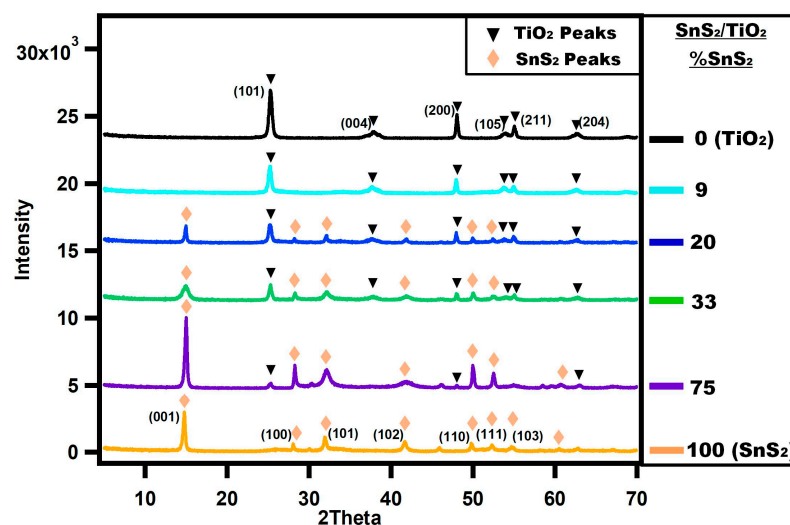
Figure 1. XRD patterns of selected SnS_2/TiO_2 composites in comparison with those of as-prepared SnS_2 and TiO_2.

The absorbance of the composites was measured by UV–vis differential reflectance spectroscopy (DRS), as shown in the inset of Figure 2. The optical bandgap of the composites was determined using the Kubelka–Munk function (Figure S2), and the results are shown as a plot as a function of %SnS_2 in Figure 2. The measured band gap of the TiO_2 nanosheets agreed well with the value in the literature (3.2 eV) for the anatase TiO_2 with an absorption edge at around 400 nm [21]. SnS_2 has an absorption edge of around 560 nm, which corresponds to a bandgap of 2.02 eV [14]. For the composites, the bandgap rapidly decreased from 3.2 eV as the %SnS_2 increased to 20%. At a higher %SnS_2, it slowly approaches that of SnS_2 (2.02 eV). This agrees well with the presence of the SnS_2 phase in the composites and the absorption by SnS_2 in the visible region with increasing %SnS_2.
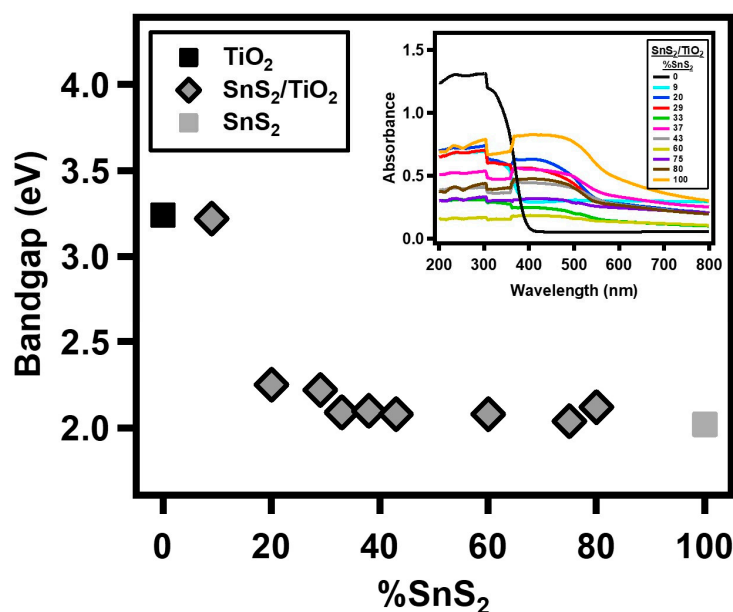
Figure 2. Bandgap of the composites as a function of %SnS_2. Also shown in the inset are the absorbance spectra of the composites.

Figure 3 shows the SEM images of the SnS_2/TiO_2 composites with various %SnS_2 ratios (c)–(e) compared to those of SnS_2 (a) and TiO_2 (b), respectively. The as-synthesized TiO_2 nanosheets show SEM images with characteristic square-shaped nanosheets (Figure 3a),

and the shape of the as-synthesized SnS_2 nanoparticles is characterized by irregularly shaped platelets (Figure 3f), confirming the 2D nature of the material. At low %SnS_2 ratios (<20%), the square-shaped TiO_2 nanosheets appear to have small nanoparticles at both the large facets and the edges of the nanosheets. It appears that the edges of the square-shaped TiO_2 nanosheets are more populated with small SnS_2 nanoparticles than the large {001} facets. In the composites with higher %SnS_2 ratios (>33%), nanoplates of different shapes that can be assigned to TiO_2 and SnS_2, respectively, are identified from the SEM images Figure 3e). It also shows that square-shaped TiO_2 nanoplates are in close contact with 2D SnS_2 platelets. With increasing %SnS_2 ratios (Figure S3), the abundant square-shaped nanosheets gradually transform into more irregularly shaped platelets, suggesting the population of SnS_2 nanoparticles increases. The EDS composition of the composites also confirms that the stoichiometric phases of SnS_2 and TiO_2 change in ratio in accordance with the varying SnS_2 mole ratios (Figure S4 and Table S1). The high oxygen content is attributed to the result of some adsorbed oxygen on the samples from the atmosphere [22]. The unique preferential distribution of SnS_2 nanoparticles at the edges of TiO_2 nanosheets may be advantageous in that the photoexcited electrons transported to the edges of TiO_2 can be consumed by the SnS_2 nanoparticles for enhanced charge separation.
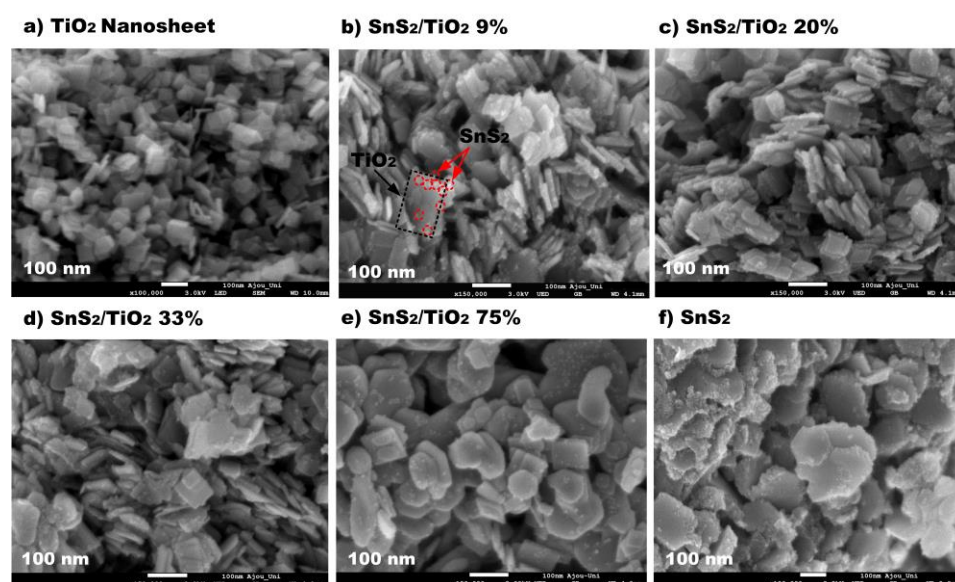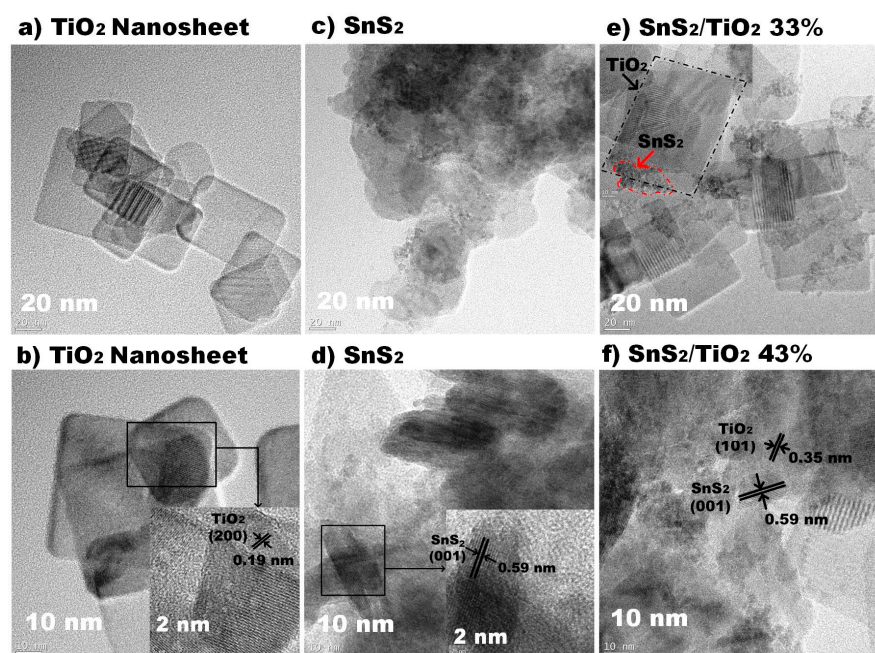

Figure 3. SEM images of (**a**) TiO_2 nanosheets, (**b**–**e**) SnS_2/TiO_2 composites with the %SnS_2 ratio of 9–75%, and (**f**) SnS_2 nanoparticles.

From Figure 4a,b, the lattice fringe of (200) planes with a lattice spacing of 0.19 nm confirms the assignment of the nanosheets to anatase TiO_2, as reported previously [23]. The TEM images of SnS_2 can be distinguished from those of TiO_2 (Figure 4a) from the characteristic irregular shapes (Figure 4c) and the distinct interplanar distance of 0.59 nm (Figure 4d) which corresponds to the d-spacing of (001) planes of hexagonal SnS_2 [24]. For the case of SnS_2/TiO_2 composites, a preferential distribution of small particles at the edges of square-shaped nanosheets can be seen (Figure 4e), suggesting that there exists a preferential chemical bonding of SnS_2 nanoparticles at the edges of the TiO_2 nanosheets. The SnS_2 nanoparticles at the edges are confirmed from the lattice fringes with an interplanar distance of 0.59 nm (Figure 4f as well as Figure S5), corresponding to the (001) facet for the 2D SnS_2 nanoparticles and the spacing of 0.35 nm which agrees well with the assignment of the {101} facet of anatase TiO_2 [5,25]. The {001} facets of TiO_2 are observed to be most exposed to the surface without being in contact with SnS_2. The edges of the anatase TiO_2 nanosheets are suggested to be the {101} facets, and the large planes are photoactive {001} facets [7,26–28]. From Figure 4e,f (as well as Figure S6), the amount of SnS_2 nanoparticles on the {001} facets of TiO_2 increases with an increase in %SnS_2. Such a change in the

distribution of SnS$_2$ nanoparticles with increasing SnS$_2$ coverage is expected to have a significant influence on the overall charge separation efficiency of the composites, as well as the charge separation mechanism at the heterojunctions.


Figure 4. TEM images of TiO$_2$ nanosheets (**a,b**), SnS$_2$ nanoparticles (**c,d**), and SnS$_2$/TiO$_2$ composites with a SnS$_2$ ratio of 33% (**e**) and 43% (**f**).

Figure 5 shows the Raman spectra of the as-synthesized SnS$_2$/TiO$_2$ composites in comparison with those of TiO$_2$ and SnS$_2$. The characteristic modes of the anatase TiO$_2$ (E$_g$, B$_{1g}$, A$_{1g}$, and E$_g$) and that of the SnS$_2$ phase (A$_{1g}$) can be identified from the spectra [14,29–31], which confirms the presence of the anatase TiO$_2$ and SnS$_2$ phases in the composites and the relative intensity ratios of the two phases vary according to the SnS$_2$ ratio. With increasing %SnS$_2$, the intensity of E$_g$ for anatase TiO$_2$ decreases, while that of the A$_{1g}$ mode for SnS$_2$ increases. The Raman spectra of all the composites are shown in Figure S7.
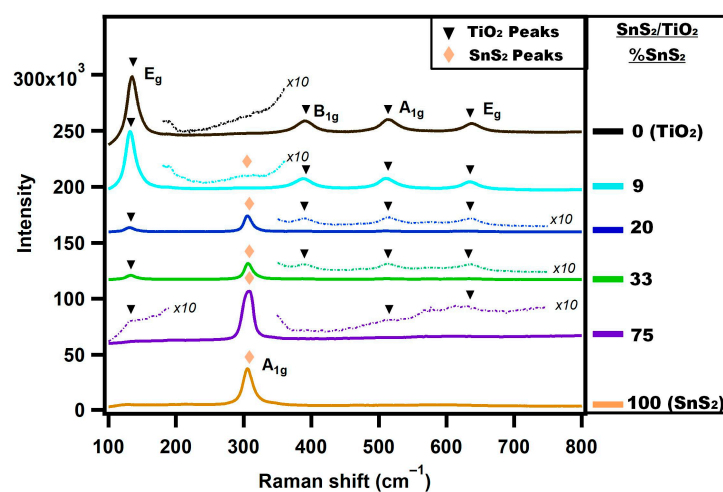
Figure 5. Raman spectra of SnS$_2$/TiO$_2$ composites in comparison with those of as-synthesis TiO$_2$ nanosheets and SnS$_2$ nanoparticles.

The photoluminescence (PL) spectra shown in Figure 6 indicate that the TiO_2 nanosheets show high PL emission at 520–550 nm under the illumination of a 325 nm laser, which is attributed to the recombination of photoexcited e^-–h^+ pairs. From Figure 6b, it can be seen that the PL intensities of the composites are dramatically lower than those of TiO_2. The PL emission rapidly drops from the very low SnS_2 ratio and approaches the minimum value at the SnS_2 ratio of about 33%. This can be interpreted as the result of the charge separation at the heterojunction between SnS_2 and TiO_2. If we assume no charge transfer between the two, the PL emission can be expected to decrease linearly from that of TiO_2 to that of pure SnS_2 (the dashed line in Figure 6b). Then, the difference between the dashed line and the actual emission can be related to the efficiency of charge separation (Figure 6c), which is the maximum up to the SnS_2 ratio of about 33%. This result demonstrates that the composites are not just a mixture of anatase TiO_2 nanosheets and SnS_2 nanoparticles but have heterojunctions that can transfer charges between them to lead to the separation of photoexcited e^-–h^+ pairs, which can lead to enhanced photocatalytic activity.
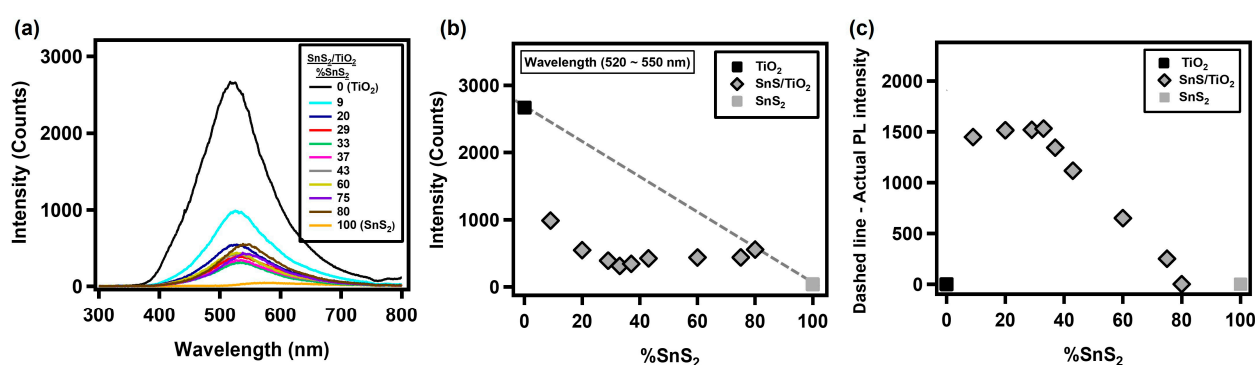
Figure 6. (**a**) PL spectra for SnS_2/TiO_2 composites with the excitation of a 325 nm laser, (**b**) the plot of maximum PL intensities at wavelengths of 520–550 nm as a function of % SnS_2, and (**c**) the plot of the difference between the dashed line (Figure 6b) and the actual emission.

XPS was employed to further interrogate the chemical bonding states in the composites. The survey spectra (Figure S8) confirm the presence of elements O, Ti, S, and Sn in the composites. The core level spectra of O 1s in Figure 7a indicate the presence of two oxygen components at 529.7 and 531.5 eV, respectively, for TiO_2, which can be assigned to lattice oxygens with direct Ti–O bonds and surface oxygen atoms in the forms of OH, respectively [32]. For the SnS_2/TiO_2 composite, the same oxygen components are observed at 530.6 and 532.4 eV, respectively, which are shifted towards higher binding energies compared to those of TiO_2. The Ti 2p core-level spectra in Figure 7b show Ti $2p_{3/2}$ and Ti $2p_{1/2}$ features at 458.6 and 464.3 eV, respectively, for TiO_2 nanosheets. The Ti $2p_{3/2}$ peak at 458.6 eV is indicative of the Ti^{4+} chemical state of stoichiometric TiO_2 [33]. The binding energies of the Ti 2p core level for SnS_2/TiO_2 also appear at 459.3 and 465.0 eV, respectively, which are shifted towards higher binding energies. Detailed fitting results of the composites further disclose the presence of an additional small Ti $2p_{3/2}$ component at lower binding energies of 456.6 eV. This may be due to Ti species with a direct Ti–S bond at the heterojunction between SnS_2 and TiO_2 [34,35]. The formation of a direct Ti–S bond at the interface can also be seen in the S 2p core-level spectra in Figure 7, which reveals a small S 2p component at the binding energies of 162.4 and 163.6 eV with the spin-orbit splitting of 1.18 eV [34,35] in addition to the major component assigned to S^{2-} of SnS_2 at 161.5 and 162.7 eV (S $2p_{3/2}$ and S $2p_{1/2}$, respectively) for SnS_2/TiO_2. For the case of SnS_2, the binding energies of S^{2-} are shown to appear at 161.8 eV and 162.9 eV for S $2p_{3/2}$ and S $2p_{1/2}$, respectively. Therefore, the binding energies of the sulfur component for SnS_2/TiO_2 are shifted towards lower binding energies than those for SnS_2. This may be the result of the heterojunction formation between SnS_2 and TiO_2 and the resulting downward (upward) shift of the electronic bands of TiO_2 (SnS_2) through an electron migration between

TiO$_2$ and SnS$_2$ in the heterojunction [33]. Sn 3d core-level spectra in Figure 7d reveal the characteristics of Sn 3d$_{3/2}$ and Sn 3d$_{5/2}$ features at 486.7 and 495.2 eV, respectively, for SnS$_2$ and SnS$_2$/TiO$_2$, which are assigned to Sn^{4+} of SnS$_2$. No distinct shift in the Sn 3d features between SnS$_2$ and SnS$_2$/TiO$_2$ can be attributed to the small shift for SnS$_2$ and the broad nature of the Sn 3d. In addition, the broad Sn 3d spectral shape of the SnS$_2$/TiO$_2$ may suggest a possible contribution of Sn–O bonding even though it is not resolved. Overall, the XPS results further indicate the heterojunction formation between SnS$_2$ and TiO$_2$ nanosheets with the formation of a direct Ti–S bond, which can be beneficial for the efficient charge transfer at the heterojunction for improvement in photoactivity.
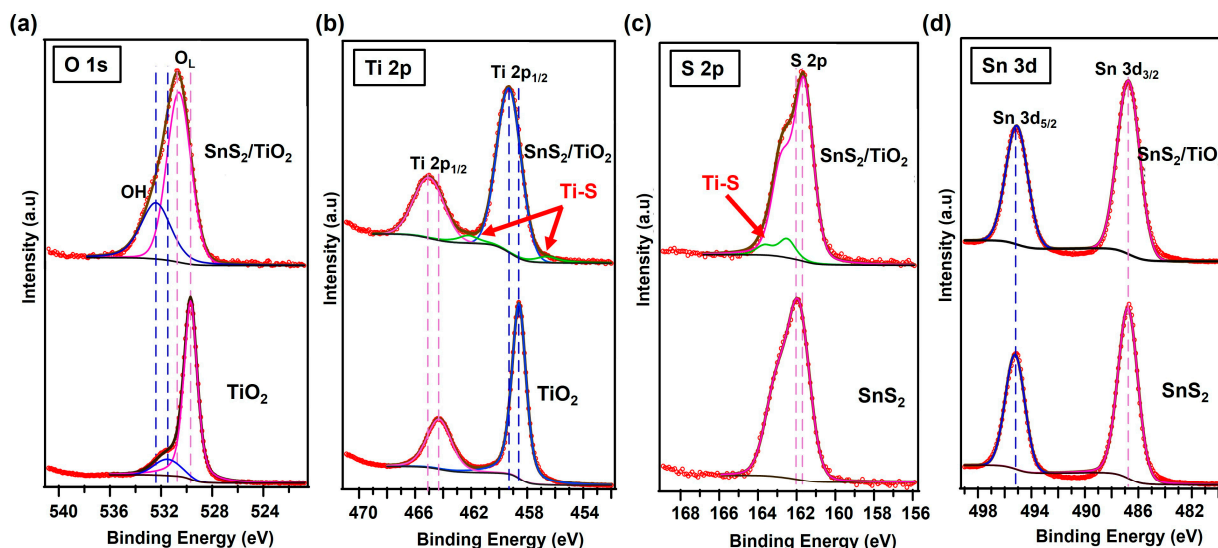

Figure 7. (**a**) O 1s, (**b**) Ti 2p, (**c**) S 2p, and (**d**) Sn 3d core-level spectra of the SnS$_2$/TiO$_2$ composite (%SnS$_2$ = 33%) in comparison with those of SnS$_2$ and TiO$_2$.

BET (Brunauer, Emmett, and Teller) N$_2$ adsorption isotherm was obtained (Figure S9a) for all the composites to evaluate the surface area since it can also provide insight into the resulting photocatalytic properties [36,37]. The measured surface areas (m^{2}g^{-1}) for the TiO$_2$ nanosheets and the SnS$_2$ nanoparticles were 61.2 and 51.2 m^{2}g^{-1}, respectively, which are in the range expected for nanoparticles of about 100 nm in diameter [38,39]. The surface area of the SnS$_2$/TiO$_2$ composites was found to be strongly dependent on the SnS$_2$ ratio (Figure S9b) and was found to be the highest (~118 m^{2}g^{-1}) at the SnS$_2$ ratios of around 33%. This result is consistent with the observation of the morphology of the composites (Figures 3 and 4), which are characterized by small SnS$_2$ nanoparticles distributed on the TiO$_2$ nanosheets. The large surface area may act as a promotional effect on the overall photocatalytic performance by providing more reaction sites.

2.2. Photoactivity of SnS$_2$/TiO$_2$ Composite

The photocatalytic activity of the composites was evaluated using the photodegradation rates of MB and RhB. The characteristic absorption bands of MB and RhB decrease in intensity as the degradation proceeds, as shown in Figure S10. From the measured variation in the intensities of the absorption bands, the C/C$_0$ was calculated and plotted against the irradiation time for MB and RhB, respectively, in Figure 8a,c. The changes in the concentration of both dye solutions with the catalyst present in the dark were limited to 3–14%, possibly due to the adsorption capacity of the catalysts (Figure S11). Assuming a first-order reaction, the initial rate constants of the composites were calculated, and the results were plotted as a function of %SnS$_2$ in Figure 8b,d for MB and RhB, respectively. The results of Figure 8 indicate that the composites exhibit higher photocatalytic performances in the photodegradation of MB and RhB, especially when the %SnS$_2$ is in the range of approximately 30%. The highest rate constant was 4.13×10^{-2} min^{-1} for MB

and 9.6×10^{-3} min^{-1} for RhB, respectively. These values for the composites are 2–3 times higher than those for anatase TiO$_2$ nanosheets and SnS$_2$ nanoparticles. The enhanced photodegradation performances of the composites are interpreted to be the result of efficient charge separation at the heterojunction of SnS$_2$ and TiO$_2$, which would result in reduced recombination rates as measured in the PL measurements (Figure 6). The large contact area between SnS$_2$ and TiO$_2$ expected for the SnS$_2$/TiO$_2$ composites with a large surface area (Figure S9) is expected to facilitate the charge transfer rate at the heterojunction to reduce the recombination rates and enhance the photodegradation rate. Photogenerated electrons within TiO$_2$ may be collected more efficiently by SnS$_2$ nanoparticles at the edges of TiO$_2$ due to the preferential diffusion of electrons towards the {101} facets of TiO$_2$ [40,41] and react with holes in the valence band (VB) of SnS$_2$ via the Z-scheme. On the other hand, small particles of SnS$_2$ may also provide recombination sites for charge carriers and limit light absorption of the anatase TiO$_2$ nanosheets to contribute to reduced photodegradation rates as well [42,43]. Therefore, the compensation between the promotional and inhibiting roles of SnS$_2$ nanoparticles may give an optimal SnS$_2$ ratio (~30%), as observed in this study. The detailed size distribution and morphologies of the SnS$_2$ nanoparticles with increasing SnS$_2$ ratios are expected to play an important role in determining the optimum SnS$_2$ ratio.
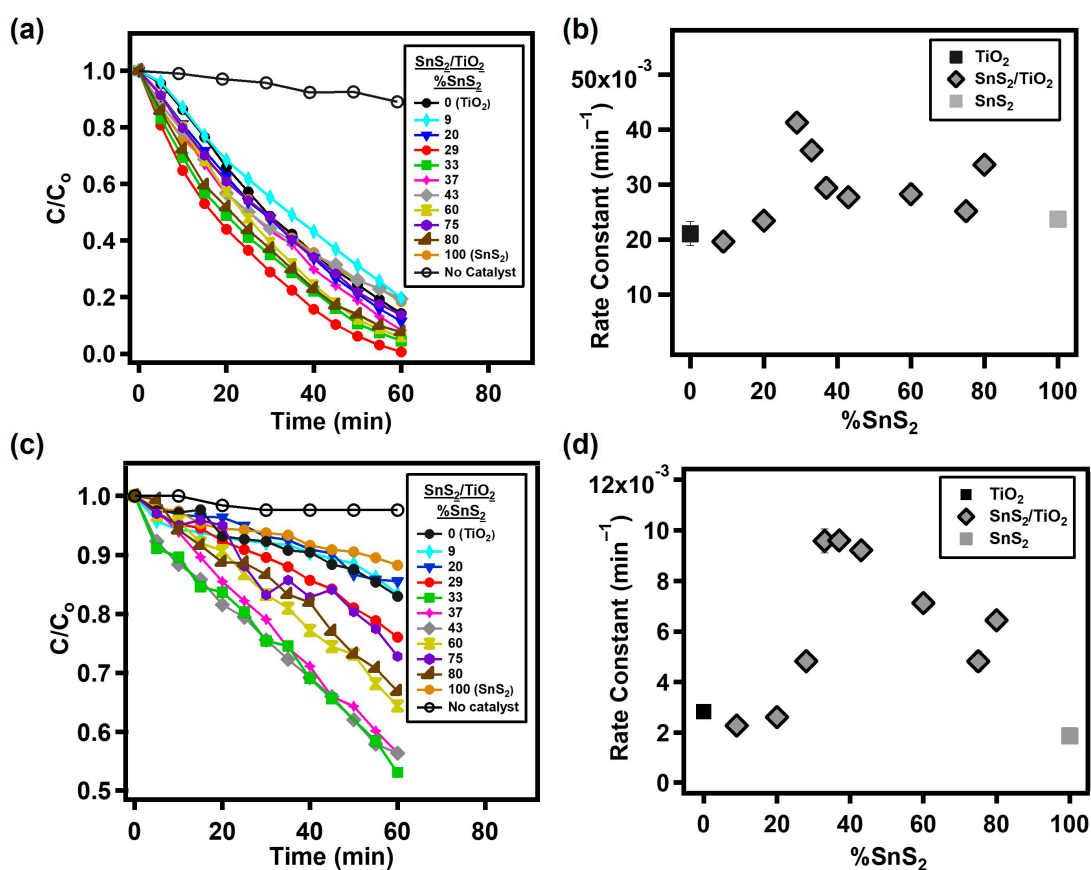
Figure 8. Photodegradation rates are shown as plots of C/Co vs. irradiation time for (**a**) MB and (**c**) RhB, along with initial rate constants vs. %SnS$_2$ in the composites for (**b**) MB and (**d**) RhB.

2.3. Proposed Mechanism for the Enhanced Photoactivity of SnS$_2$/TiO$_2$ Composite

To further investigate the degradation mechanism and the role of SnS$_2$/TiO$_2$ heterojunction, we employed scavengers such as 1,4 benzoquinone (for $\bullet O_2^-$) [44,45], isopropyl alcohol (for $\bullet OH$) [46,47], sodium oxalate (for h$^+$) [21,48], and silver nitrate (for e$^-$) [49,50] and the changes in the photodegradation rates were evaluated (Figure S12) and compared as shown in Figure 9. The decrease in the degradation rate with the addition of the scavenger indicates that the associated hot carrier plays a dominant role in the

photodegradation reaction. For the SnS_2/TiO_2 composites with the optimized SnS_2 content (~30%), the results indicate that the rate constant generally decreases when scavengers are added, suggesting that all active species play a role in the photodegradation of the dyes. The impact of adding 1,4 benzoquinone (for $\bullet O_2^-$) and silver nitrate (for e^-) was found to be a dramatic decrease of approximately 70–90%, while the influences of isopropyl alcohol (for $\bullet OH$) and sodium oxalate (for h^+) were relatively limited to a small decrease of approximately 10–30%. Such trends were found to be consistent for both MB and RhB, as can be seen in Figure 9, suggesting that e^- and $\bullet O_2^-$ play a major role in the photodegradation of the dyes.
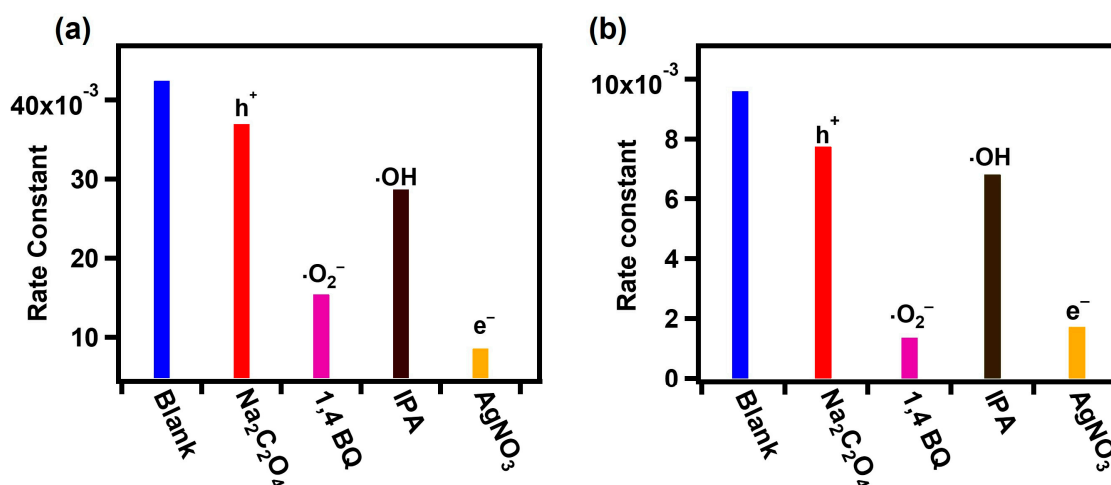
Figure 9. Comparison of rate constants with the use of trapping agents for (**a**) MB (SnS_2/TiO_2 29%) and (**b**) RhB (SnS_2/TiO_2 33%).

Considering that the E_{CB} and E_{VB} for SnS_2 (-0.82 eV and 1.17 eV vs. NHE, respectively) are more negative than those of anatase TiO_2 nanosheet (-0.31 eV and 2.93 eV vs. NHE, respectively), the heterojunction could be either type II heterojunction or direct Z-scheme [51]. Composite systems with SnS_2 and TiO_2 heterojunctions listed in Table 1 were also proposed to follow either type II heterojunction or direct Z-scheme, depending on the detailed preparation and evaluation conditions. Nonetheless, the E_{VB} of SnS_2 is more negative than the standard redox potential of $E°(\cdot OH/OH^-) = 1.99$ eV (vs. NHE) [52], implying that the photogenerated holes of SnS_2 may not be able to oxidize OH^- to yield $\cdot OH$ radicals [52,53]. To confirm this, trapping experiments were carried out for TiO_2 nanosheet and SnS_2 using sodium oxalate (for h^+) and silver nitrate (for e^-) (Figure S13). The hot carriers (h^+ and e^-) of TiO_2 were found to play an important role in the degradation of the dye, as can be expected from the proposed energy diagram of Figure 10. The effect of trapping e^- was also a significant reduction in the degradation rate, as can be expected from the sufficiently high reducing power of the e^- in the CB of SnS_2. However, the capture of h^+ in SnS_2 was found to slightly increase the degradation rate, which can be interpreted as the role of the h^+-scavenger was the suppression of the recombination rate within SnS_2. This is consistent with the above energy diagram and confirms that the photogenerated holes of SnS_2 may not be effective in oxidizing OH^- to yield $\cdot OH$ radicals. Contrary to the case of SnS_2, the scavenger experiments for the SnS_2/TiO_2 composites (Figure 9) clearly show that the h^+ and $\cdot OH$ radicals contribute to the photodegradation of the dyes. Therefore, the most likely charge transfer pathway at the heterojunction is likely to be the direct Z-scheme, as has been reported for studies of 2D–2D SnS_2/TiO_2 [42]. SnS_2 nanoparticles preferentially bound at the {101} edges of TiO_2 nanosheets can collect electrons more favorably from TiO_2 to promote Z-scheme interaction. Similar charge transfer mechanisms have been reported for other composite systems, such as $SnS_2/BiOBr$ [53] and g-C_3N_4/Vo-ZnO [52].
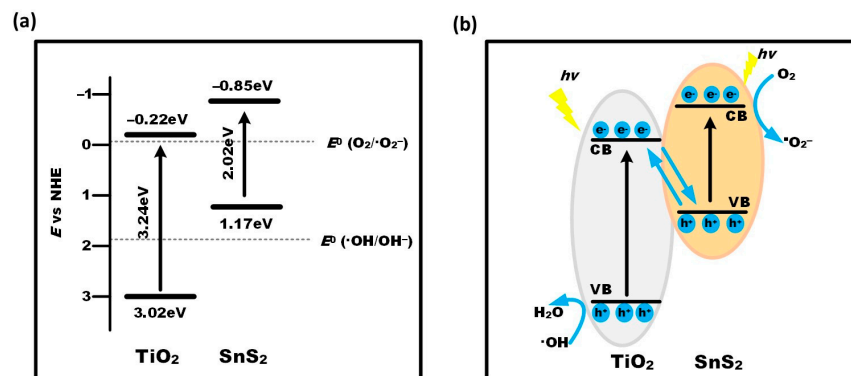
Figure 10. Energy diagram of the valence band (VB) and conduction band (CB) of the SnS_2/TiO_2 composite and a plausible mechanism for the charge separation and the generation of radical species. (**a**) Band alignment diagram for the SnS_2/TiO_2 and (**b**) Proposed charge separation mechanism at the heterojunction via Z-scheme. The energy levels for the CB (E_{CB}) and the VB (E_{VB}) can be calculated following Equations (S1) and (S2) listed in the Supplementary Materials.

That being the case, under light irradiation, both the TiO_2 nanosheet and SnS_2 absorb photons and generate electron−hole pairs with electrons excited to their respective conduction bands. The electrons accumulated in the conduction band of SnS_2 with a strong reduction potential can react with O_2 to form $\bullet O_2^-$ because E_{CB} of SnS_2 is more negative than $E°(O_2/\bullet O_2^-) = -0.046$ eV (vs. NHE) [52]. Meanwhile, the photoinduced electrons in the TiO_2 conduction band can recombine with the holes in the valence band of SnS_2. Finally, the holes in the valence band of the TiO_2 nanosheet with its high positive potential ($E_{VB} = 3.02$ eV) can oxidize MB. This charge transfer pathway would effectively enhance charge separation while retaining its great oxidation and reduction abilities [51]. Although the degradation products were not determined in this study, the subsequent degradation of both dyes was suggested to undergo the following pathways. The degradation of RhB was suggested to be initiated by the removal of ethyl groups, resulting in intermediate products such as phthalic acid, benzyloxyamine, and benzoic acid [54]. Similarly, the degradation of MB was suggested to begin with the removal of methyl groups, resulting in the formation of intermediates such as N-methyl formamide, azure A, B, and C, as well as thionine [55–57].

Table 1. Proposed type of heterojunction and degradation performances of SnS_2/TiO_2 photocatalysts.

| System	Type of Heterojunction	Catalyst Concentration (g/L)	Dye (Concentration)	Light Source	Rate Constant (min⁻¹)	Reference
SnS_2/TiO_2	Z-scheme	0.02	MB (7.5 μM) and RhB (3.75 mg/L)	Halogen lamb (100 mW/cm²)	0.052 (MB) 0.008 (RhB)	This work
SnS_2/TiO_2	Z-scheme	0.15	MB (12 μM) and RhB (10 mg/L)	Xe lamp (200 W, 200–800 nm)	0.02 (MB) 0.022 (RhB)	Gao et al. (2021) [58]
SnS_2/TiO_2	Type II	0.2	MB (20 μM)	Mercury lamp (250 W)	0.03	Zhang et al. (2017) [56]
$TiO_2/SnS_2/MoS_2$	Z-scheme	-	MB (10 mL, 5 mg/L)	Artificial sunlight (AM 1.5 G, 150 mW)	0.0175	Gao et al. (2022) [59]
SnS_2/TiO_2	Type II	1	RhB (10 mg/L)	Xe lamp (300 W, 420 nm)	0.035	Yan et al. (2017) [60]
$SnS_2/BiOBr$	Z-scheme	0.625	RhB (10 mg/L)	Xe lamp (400 W, 420 nm)	0.1203	Qiu et al. (2017) [53]
SnS_2/TiO_2	Z-scheme	50	CO_2	Xe lamp (300 W)	-	She et al. (2019) [42]
TiO_2/CdS	Z-scheme	2	CO_2	Xe lamp (350 W)	-	Wang et al. (2020) [61]

3. Materials and Methods

3.1. Synthesis of TiO$_2$ Nanosheets

The detailed procedures for the preparation of the anatase TiO$_2$ nanosheet were described in our previous work [27]. Butanol (25 mL) and tetrabutyl titanate (TBT, 25 g) were added into a Teflon beaker and kept in an ice bath under stirring. Then, 4 mL of HF was subsequently added dropwise, and the resulting solution was transferred into a Teflon-lined autoclave, which was firmly screwed tight and kept in an oven at 200 °C for 24 h. After the reaction, the precipitate was filtered, washed with deionized water, and dried at 80 °C.

3.2. Synthesis of SnS$_2$/TiO$_2$

The as-synthesized TiO$_2$ nanosheet (0.2 g) was dispersed in 40 mL of deionized water and stirred for 1 h using a high-power sonicator (VC505, Sonics & Materials, Newtown, CT, USA). Then, an aqueous solution of SnCl$_4$·5H$_2$O and CH$_3$CSNH$_2$ (with the Sn-to-S mole ratio of 1:2) was mixed with the aqueous suspension of TiO$_2$ with initial mixing mole ratios of Sn from 9 to 80%. The mixture was stirred for 1 h and placed on a microwave synthesizer (Monowave 400, Anton Paar, Graz, Austria) operating at 850 W, 200 °C, and stirring at 900 rpm for 1-h synthesis. The schematic of the whole procedure is shown in Scheme 1.
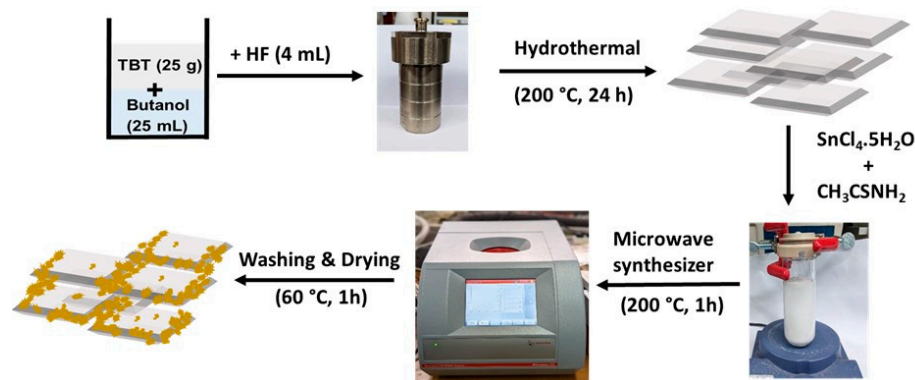
Scheme 1. The schematic diagram for the synthesis of SnS$_2$/TiO$_2$ heterojunction.

3.3. Characterization of As-Synthesized Photocatalysts

The detailed morphologies of the as-synthesized composites were examined by transmission electron microscopy (TEM, Tecnai G2 F30 S-Twin, Igualada, España) and scanning electron microscopy (SEM, JSM-7900F, JEOL, Tokyo, Japan). Diffuse reflectance spectra were measured with a UV–visible spectrophotometer (Scinco, Neosys-2000, Seoul, Republic of Korea) that was equipped with an integrating sphere and BaSO$_4$ as the reference. X-ray diffraction (XRD) patterns of our samples were measured with Cu Kα radiation from an X-ray diffractometer (Rigaku, Ultima III, Tokyo, Japan). X-ray photoelectron spectroscopy (XPS) measurement was performed using K-alpha (Thermo VG, Altrincham, UK) with monochromated Al X-ray sources (Al Kα line: 1486.6 eV). All binding energies are calibrated to the C 1s peak at 284.8 eV of the adventitious carbon on the surface.

3.4. Evaluation of Photocatalytic Properties

The photodegradation characteristics of the composites were evaluated using MB and RhB as model dyes. 10 mL of the aqueous solution of MB or RhB (6×10^{-5} M) was added to 40 mL of the aqueous solution with SnS$_2$/TiO$_2$ composites (0.04 g/L), which were diluted with 30 mL of distilled H$_2$O to result in 80 mL aqueous solution. The solution was stirred in the dark for 60 min before light illumination to achieve adsorption–desorption equilibrium of the MB and RhB dyes. Photocatalytic reactions were initiated with a halogen lamp (100 mW/cm^2). During light illumination, the air was constantly blown by a fan to mitigate any temperature rise from room temperature. For the investigation of the role of

hot carriers, the aqueous solution (5 mL, 20 mM) of the scavengers (1,4 benzoquinone (for $\bullet O_2{}^-$), isopropyl alcohol (for $\bullet OH$), sodium oxalate (for h^+), and silver nitrate (for e^-)) was added to the solution before shining light. The solution was sampled during the reaction to determine the concentration of MB (or RhB) from the absorbance at 664 (555) nm for MB (RhB). Initial rate constants for the photodegradation reactions were obtained by assuming first-order reaction kinetics.

4. Conclusions

A microwave-assisted hydrothermal method was employed to synthesize SnS_2/TiO_2 composites for photocatalytic applications. Both TiO_2 nanosheets and SnS_2 nanoparticles showed activities in the photodegradation of MB and RhB. Such activities were found to be further enhanced for the SnS_2/TiO_2 composites, especially when the SnS_2 ratio in the composite was around 30%, giving an overall volcano-type change in the graph of the photodegradation performances of the composites vs. the SnS_2 ratio. The origin of the enhanced photocatalytic activity is attributed to the formation of SnS_2–TiO_2 heterojunctions, which can facilitate the charge separation to reduce the recombination rate. The composites with the maximum photocatalytic performances (in the SnS_2 ratio of about 30%) have small SnS_2 nanoparticles in contact with the TiO_2 nanosheets, especially at the edges of the nanosheets, which can result in a large surface area of the composites (~118 m^2g^{-1}) and the large interfacial heterojunction for efficient charge separation following the Z-scheme towards enhanced photocatalytic performances. The preferential diffusion of electrons toward the edges of the TiO_2 nanosheets may facilitate the charge separation at the SnS_2 heterojunctions at the {101} edges of TiO_2 via Z-scheme further. Scavenger experiments further corroborate the charge transfer mechanism at the interfaces following Z-scheme, suggesting that the SnS_2/TiO_2 composites can be good examples of promising photocatalysts for the photodegradation of dyes with enhanced redox ability.

Supplementary Materials: The following supporting information can be downloaded at https://www.mdpi.com/article/10.3390/catal14070442/s1, Figure S1. XRD patterns of as-prepared SnS_2, TiO_2 nanosheet, and SnS_2/TiO_2 heterojunction. Figure S2. Bandgap energy plot Kubelka–Munk function for synthesis samples. Figure S3. a–i shows SEM images of SnS_2/TiO_2 heterojunctions. Figure S4. a–i shows EDS images of SnS_2/TiO_2 heterojunctions. Figure S5. Profile of inverse fast Fourier transformation (IFFT) for (a) anatase TiO_2 nanosheet (200), (b) SnS_2 nanoparticles (001), (c) SnS_2/TiO_2 43% (TiO_2 (101) and SnS_2 (001), respectively). Figure S6. Increase content of SnS_2 nanoparticles for (a) SnS_2/TiO_2 33% and (b) SnS_2/TiO_2 43%. Figure S7. Raman spectra patterns of as-synthesis TiO_2 nanosheets, SnS_2 nanoparticles, and SnS_2/TiO_2 heterojunctions. Figure S8. Survey scan spectra of synthesis samples. Figure S9. (a) BET N_2 adsorption isotherms and (b) the measured surface area of the SnS_2/TiO_2 composites, SnS_2, and TiO_2. Figure S10. Typical absorbance for a) MB and b) RhB degradation under halogen lamp irradiation in the presence of SnS_2/TiO_2 shows a decrease in absorbance peak with time. Figure S11. Photodegradation rates are shown as plots of C/Co vs. time in the dark for (a) MB and (b) RhB. Figure S12. C/C_0 for trapping experiment using MB (SnS_2/TiO_2 29%) and RhB (SnS_2/TiO_2 33%). Figure S13. Rate constant for trapping experiment for using MB TiO_2 and SnS_2. Table S1. %SnS_2 calculations from EDS data. References [62–64] are cited in the Supplementary Materials.

Author Contributions: N.C.: writing—original draft, investigation, visualization, formal analysis. M.F.: visualization, formal analysis. H.-S.O.: investigation, formal analysis. Y.-K.K.: conceptualization, formal analysis, writing—original draft, writing—review and editing, project administration, funding acquisition. All authors have read and agreed to the published version of the manuscript.

Data Availability Statement: Data are contained within the article and Supplementary Materials.

Conflicts of Interest: The authors declare that they have no known competing financial interests or personal relationships that could have appeared to influence the work reported in this paper.

References

1. Kumari, H.; Sonia; Suman; Ranga, R.; Chahal, S.; Devi, S.; Sharma, S.; Kumar, S.; Kumar, P.; Kumar, S.; et al. A review on photocatalysis used for wastewater treatment: Dye degradation. *Water Air Soil Pollut.* **2023**, *234*, 349. [CrossRef]
2. Sultana, R.; Liba, S.I.; Rahman, M.A.; Yeachin, N.; Syed, I.M.; Bhuiyan, M.A. Enhanced photocatalytic activity in RhB dye degradation by Mn and B co-doped mixed phase TiO_2 photocatalyst under visible light irradiation. *Surf. Interfaces* **2023**, *42*, 103302. [CrossRef]
3. Fujishima, A.; Honda, K. Electrochemical photolysis of water at a semiconductor electrode. *Nature* **1972**, *238*, 37–38. [CrossRef]
4. Yu, X.; Jeon, B.; Kim, Y.K. Dominant influence of the surface on the photoactivity of shape-controlled anatase TiO_2 nanocrystals. *ACS Catal.* **2015**, *5*, 3316–3322. [CrossRef]
5. Wu, B.; Guo, C.; Zheng, N.; Xie, Z.; Stucky, G.D. Nonaqueous production of nanostructured anatase with high-energy facets. *J. Am. Chem. Soc.* **2008**, *130*, 17563–17567. [CrossRef]
6. Yu, J.; Fan, J.; Lv, K. Anatase TiO_2 nanosheets with exposed (001) facets: Improved photoelectric conversion efficiency in dye-sensitized solar cells. *Nanoscale* **2010**, *2*, 2144–2149. [CrossRef]
7. Wen, C.Z.; Jiang, H.B.; Qiao, S.Z.; Yang, H.G.; Lu, G.Q. Synthesis of high-reactive facets dominated anatase TiO_2. *J. Mater. Chem.* **2011**, *21*, 7052–7061. [CrossRef]
8. Zhang, H.; Sun, P.; Fei, X.; Wu, X.; Huang, Z.; Zhong, W.; Gong, Q.; Zheng, Y.; Zhang, Q.; Xie, S.; et al. Unusual facet and co-catalyst effects in TiO_2-based photocatalytic coupling of methane. *Nat. Commun.* **2024**, *15*, 4453. [CrossRef]
9. Ozawa, K.; Emori, M.; Yamamoto, S.; Yukawa, R.; Yamamoto, S.; Hobara, R.; Fujikawa, K.; Sakama, H.; Matsuda, I. Electron–hole recombination time at TiO_2 single-crystal surfaces: Influence of surface band bending. *J. Phys. Chem. Lett.* **2014**, *5*, 1953–1957. [CrossRef]
10. Wang, Y.; Fiaz, M.; Kim, J.; Carl, N.; Kim, Y.K. Kinetic evidence for type-II heterojunction and z-scheme interactions in g-C_3N_4/TiO_2 nanotube-based photocatalysts in photocatalytic hydrogen evolution. *ACS Appl. Energy Mater.* **2023**, *6*, 5197–5206. [CrossRef]
11. Govinda Raj, M.; Mahalingam, S.; Gnanarani, S.V.; Jayashree, C.; Ganeshraja, A.S.; Pugazhenthiran, N.; Rahaman, M.; Abinaya, S.; Senthil, B.; Kim, J. TiO_2 nanorod decorated with MoS_2 nanospheres: An efficient dual-functional photocatalyst for antibiotic degradation and hydrogen production. *Chemosphere* **2024**, *357*, 142033. [CrossRef]
12. Yang, S.; Lu, Q.; Wang, F.; Zhi, Y.; Chen, J.; Wang, Y.; Zhang, H.; Yin, H.; Sun, P.; Cao, W. S-scheme SnO/TiO_2 heterojunction with high hole mobility for boosting photocatalytic degradation of gaseous benzene. *Chem. Eng. J.* **2023**, *478*, 147345. [CrossRef]
13. Pandeya, S.; Ding, R.; Ma, Y.; Han, X.; Gui, M.; Mulmi, P.; Panthi, K.P.; Neupane, B.B.; Pant, H.R.; Li, Z.; et al. Self-standing CdS/TiO_2 Janus nanofiberous membrane: COD removal, antibacterial activity and photocatalytic degradation of organic pollutants. *J. Environ. Chem. Eng.* **2024**, *12*, 112521. [CrossRef]
14. Burton, L.A.; Whittles, T.J.; Hesp, D.; Linhart, W.M.; Skelton, J.M.; Hou, B.; Webster, R.F.; O'Dowd, G.; Reece, C.; Cherns, D.; et al. Electronic and optical properties of single crystal SnS_2: An earth-abundant disulfide photocatalyst. *J. Mater. Chem. A* **2016**, *4*, 1312–1318. [CrossRef]
15. Zhang, F.; Zhang, Y.; Wang, Y.; Zhu, A.; Zhang, Y. Efficient photocatalytic reduction of aqueous Cr (VI) by Zr^{4+} doped and polyaniline coupled SnS_2 nanoflakes. *Sep. Purif. Technol.* **2022**, *283*, 120161. [CrossRef]
16. Nguyen Thi, T.H.; Huu, H.T.; Phi, H.N.; Nguyen, V.P.; Le, Q.D.; Thi, L.N.; Trang Phan, T.T.; Vo, V. A facile synthesis of SnS_2/g-C_3N_4 S-scheme heterojunction photocatalyst with enhanced photocatalytic performance. *J. Sci. Adv. Mater. Devices* **2022**, *7*, 100402. [CrossRef]
17. Xie, Q.; Zhou, H.; Lv, Z.; Liu, H.; Guo, H. Sn^{4+} self-doped hollow cubic SnS as an efficient visible-light photocatalyst for Cr(VI) reduction and detoxification of cyanide. *J. Mater. Chem. A* **2017**, *5*, 6299–6309. [CrossRef]
18. Zhu, L.; Lu, Q.; Lv, L.; Wang, Y.; Hu, Y.; Deng, Z.; Lou, Z.; Hou, Y.; Teng, F. Ligand-free rutile and anatase TiO_2 nanocrystals as electron extraction layers for high performance inverted polymer solar cells. *RSC Adv.* **2017**, *7*, 20084–20092. [CrossRef]
19. Wang, M.; Tan, S.; Kan, S.; Wu, Y.; Sang, S.; Liu, K.; Liu, H. In-situ assembly of TiO_2 with high exposure of (001) facets on three-dimensional porous graphene aerogel for lithium-sulfur battery. *J. Energy Chem.* **2020**, *49*, 316–322. [CrossRef]
20. Huang, G.; Zhang, J.; Jiang, F.; Zhang, Z.; Zeng, J.; Qi, X.; Shen, Z.; Wang, H.; Kong, Z.; Xi, J.; et al. Excellent photoelectrochemical activity of Bi_2S_3 nanorod/TiO_2 nanoplate composites with dominant {001} facets. *J. Solid State Chem.* **2020**, *281*, 121041. [CrossRef]
21. Gonçalves, B.S.; Palhares, H.G.; Souza, T.C.C.d.; Castro, V.G.d.; Silva, G.G.; Silva, B.C.; Krambrock, K.; Soares, R.B.; Lins, V.F.C.; Houmard, M.; et al. Effect of the carbon loading on the structural and photocatalytic properties of reduced graphene oxide-TiO_2 nanocomposites prepared by hydrothermal synthesis. *J. Mater. Res. Technol.* **2019**, *8*, 6262–6274. [CrossRef]
22. Mayerhofer, A.; Dali, Y.; Presoly, P.; Bernhard, C.; Michelic, S.K. Study on the possible error due to matrix interaction in automated SEM/EDS analysis of nonmetallic inclusions in steel by thermodynamics, kinetics and electrolytic extraction. *Metals* **2020**, *10*, 860. [CrossRef]

23. Yuan, Y.-J.; Ye, Z.-J.; Lu, H.-W.; Hu, B.; Li, Y.-H.; Chen, D.-Q.; Zhong, J.-S.; Yu, Z.-T.; Zou, Z.-G. Constructing anatase TiO_2 nanosheets with exposed (001) facets/layered MoS_2 two-dimensional nanojunctions for enhanced solar hydrogen generation. *ACS Catal.* **2016**, *6*, 532–541. [CrossRef]

24. Dashairya, L.; Sharma, M.; Basu, S.; Saha, P. SnS_2/RGO based nanocomposite for efficient photocatalytic degradation of toxic industrial dyes under visible-light irradiation. *J. Alloys Compd.* **2019**, *774*, 625–636. [CrossRef]

25. Ye, L.; Mao, J.; Liu, J.; Jiang, Z.; Peng, T.; Zan, L. Synthesis of anatase TiO_2 nanocrystals with {101}, {001} or {010} single facets of 90% level exposure and liquid-phase photocatalytic reduction and oxidation activity orders. *J. Mater. Chem. A* **2013**, *1*, 10532–10537. [CrossRef]

26. Selcuk, S.; Selloni, A. Facet-dependent trapping and dynamics of excess electrons at anatase TiO_2 surfaces and aqueous interfaces. *Nat. Mater.* **2016**, *15*, 1107–1112. [CrossRef]

27. Yu, X.; Wang, Y.; Kim, Y.K. Engineering defects and photocatalytic activity of TiO_2 nanoparticles by thermal treatments in NH_3 and subsequent surface chemical etchings. *Phys. Chem. Chem. Phys.* **2017**, *19*, 24049–24058. [CrossRef]

28. Lee, T.-Y.; Lee, C.-Y.; Chiu, H.-T. Enhanced photocatalysis from truncated octahedral bipyramids of anatase TiO_2 with exposed {001}/{101} facets. *ACS Omega* **2018**, *3*, 10225–10232. [CrossRef]

29. Sriv, T.; Kim, K.; Cheong, H. Low-frequency raman spectroscopy of few-layer $2H$-SnS_2. *ACS Catal.* **2018**, *8*, 10194. [CrossRef]

30. Tian, F.; Zhang, Y.; Zhang, J.; Pan, C. Raman spectroscopy: A new approach to measure the percentage of anatase TiO_2 exposed (001) facets. *J. Phys. Chem. C* **2012**, *116*, 7515–7519. [CrossRef]

31. Du, Y.L.; Deng, Y.; Zhang, M.S. Variable-temperature raman scattering study on anatase titanium dioxide nanocrystals. *J. Phys. Chem. Solids* **2006**, *67*, 2405–2408. [CrossRef]

32. Sun, L.; Zhao, Z.; Li, S.; Su, Y.; Huang, L.; Shao, N.; Liu, F.; Bu, Y.; Zhang, H.; Zhang, Z. Role of SnS_2 in 2D–2D SnS_2/TiO_2 nanosheet heterojunctions for Photocatalytic Hydrogen Evolution. *ACS Appl. Nano Mater.* **2019**, *2*, 2144–2151. [CrossRef]

33. Sun, Q.; Li, Y.; Hao, J.; Zheng, S.; Zhang, T.; Wang, T.; Wu, R.; Fang, H.; Wang, Y. Increased active sites and charge transfer in the SnS_2/TiO_2 heterostructure for visible-light-assisted NO_2 sensing. *ACS Appl. Mater. Interfaces* **2021**, *13*, 54152–54161. [CrossRef] [PubMed]

34. van Kasteren, J.G.A.; Basuvalingam, S.B.; Mattinen, M.; Bracesco, A.E.A.; Kessels, W.M.M.; Bol, A.A.; Macco, B. Growth mechanism and Film properties of atomic-layer-deposited titanium oxysulfide. *Chem. Mater.* **2022**, *34*, 7750–7760. [CrossRef]

35. Gonbeau, D.; Guimon, C.; Pfister-Guillouzo, G.; Levasseur, A.; Meunier, G.; Dormoy, R. XPS study of thin films of titanium oxysulfides. *Surf. Sci.* **1991**, *254*, 81–89. [CrossRef]

36. He, Z.; Que, W. Surface scattering and reflecting: The effect on light absorption or photocatalytic activity of TiO_2 scattering microspheres. *Phys. Chem. Chem. Phys.* **2013**, *15*, 16768–16773. [CrossRef] [PubMed]

37. He, Z.; Zhu, Z.; Li, J.; Zhou, J.; Wei, N. Characterization and activity of mesoporous titanium dioxide beads with high surface areas and controllable pore sizes. *J. Hazard. Mater.* **2011**, *190*, 133–139. [CrossRef] [PubMed]

38. Yadav, U. 2D SnS_2 nanostructure-derived photocatalytic degradation of organic pollutants under visible Light. *Front. Nanotechnol.* **2021**, *3*, 711368. [CrossRef]

39. Veres, Á.; Ménesi, J.; Janáky, C.; Samu, G.F.; Scheyer, M.K.; Xu, Q.; Salahioglu, F.; Garland, M.V.; Dékány, I.; Zhong, Z. New insights into the relationship between structure and photocatalytic properties of TiO_2 catalysts. *RSC Adv.* **2015**, *5*, 2421–2428. [CrossRef]

40. Hou, L.; Guan, Z.; Liu, T.; He, C.; Li, Q.; Yang, J. Synergistic effect of {101} crystal facet and bulk/surface oxygen vacancy ratio on the photocatalytic hydrogen production of TiO_2. *Int. J. Hydrogen Energy* **2019**, *44*, 8109–8120. [CrossRef]

41. Roy, N.; Sohn, Y.; Pradhan, D. Synergy of low-energy {101} and high-energy {001} TiO_2 crystal facets for enhanced photocatalysis. *ACS Nano* **2013**, *7*, 2532–2540. [CrossRef] [PubMed]

42. She, H.; Zhou, H.; Li, L.; Zhao, Z.; Jiang, M.; Huang, J.; Wang, L.; Wang, Q. Construction of a two-dimensional composite derived from TiO_2 and SnS_2 for enhanced photocatalytic reduction of CO_2 into CH_4. *ACS Sustain. Chem. Eng.* **2019**, *7*, 650–659. [CrossRef]

43. Chen, Z.; Wang, W.; Zhang, Z.; Fang, X. High-efficiency visible-light-driven Ag_3PO_4/AgI photocatalysts: Z-scheme photocatalytic mechanism for their enhanced photocatalytic activity. *J. Phys. Chem. C* **2013**, *117*, 19346–19352. [CrossRef]

44. Ding, X.; Zhao, K.; Zhang, L. Enhanced photocatalytic removal of sodium pentachlorophenate with self-doped Bi_2WO_6 under visible light by generating more superoxide ions. *Environ. Sci. Technol.* **2014**, *48*, 5823–5831. [CrossRef] [PubMed]

45. Ren, B.; Wang, T.; Qu, G.; Deng, F.; Liang, D.; Yang, W.; Liu, M. In situ synthesis of g-C_3N_4/TiO_2 heterojunction nanocomposites as a highly active photocatalyst for the degradation of Orange II under visible light irradiation. *Environ. Sci. Pollut. Res.* **2018**, *25*, 19122–19133. [CrossRef] [PubMed]

46. Shanmugaratnam, S.; Selvaratnam, B.; Baride, A.; Koodali, R.; Ravirajan, P.; Velauthapillai, D.; Shivatharsiny, Y. SnS_2/TiO_2 nanocomposites for hydrogen production and photodegradation under extended solar irradiation. *Catalysts* **2021**, *11*, 589. [CrossRef]

47. He, Y.; Zhang, L.; Fan, M.; Wang, X.; Walbridge, M.L.; Nong, Q.; Wu, Y.; Zhao, L. Z-scheme SnO_{2-x}/g-C_3N_4 composite as an efficient photocatalyst for dye degradation and photocatalytic CO_2 reduction. *Sol. Energy Mater. Sol. Cells* **2015**, *137*, 175–184. [CrossRef]

48. Ju, L.; Wu, P.; Yang, Q.; Ahmed, Z.; Zhu, N. Synthesis of ZnAlTi-LDO supported C_{60}@AgCl nanoparticles and their photocatalytic activity for photo-degradation of Bisphenol A. *Appl. Catal. B Environ.* **2018**, *224*, 159–174. [CrossRef]

49. Moss, B.; Lim, K.K.; Beltram, A.; Moniz, S.; Tang, J.; Fornasiero, P.; Barnes, P.; Durrant, J.; Kafizas, A. Comparing photoelectro-chemical water oxidation, recombination kinetics and charge trapping in the three polymorphs of TiO_2. *Sci. Rep.* **2017**, *7*, 2938. [CrossRef] [PubMed]

50. Bechambi, O.; Chalbi, M.; Najjar, W.; Sayadi, S. Photocatalytic activity of ZnO doped with Ag on the degradation of endocrine disrupting under UV irradiation and the investigation of its antibacterial activity. *Appl. Surf. Sci.* **2015**, *347*, 414–420. [CrossRef]

51. Su, Q.; Li, Y.; Hu, R.; Song, F.; Liu, S.; Guo, C.; Zhu, S.; Liu, W.; Pan, J. Heterojunction photocatalysts based on 2D materials: The role of configuration. *Adv. Sustain. Syst.* **2020**, *4*, 2000130. [CrossRef]

52. Liu, Y.; Wang, R.; Yang, Z.; Du, H.; Jiang, Y.; Shen, C.; Liang, K.; Xu, A. Enhanced visible-light photocatalytic activity of Z-scheme graphitic carbon nitride/oxygen vacancy-rich zinc oxide hybrid photocatalysts. *Chin. J. Catal.* **2015**, *36*, 2135–2144. [CrossRef]

53. Qiu, F.; Li, W.; Wang, F.; Li, H.; Liu, X.; Sun, J. In-situ synthesis of novel Z-scheme SnS_2/BiOBr photocatalysts with superior photocatalytic efficiency under visible light. *J. Colloid Interface Sci.* **2017**, *493*, 1–9. [CrossRef] [PubMed]

54. Sharma, S.; Mittal, A.; Chauhan, N.S.; Saini, S.; Yadav, J.; Kushwaha, M.; Chakraborty, R.; Sengupta, S.; Kumari, K.; Kumar, N. Mechanistic investigation of RhB photodegradation under low power visible LEDs using a Pd-modified TiO2/Bi2O3 photocatalyst: Experimental and DFT studies. *J. Phys. Chem. Solids* **2022**, *162*, 110510. [CrossRef]

55. Rauf, M.A.; Meetani, M.A.; Khaleel, A.; Ahmed, A. Photocatalytic degradation of Methylene Blue using a mixed catalyst and product analysis by LC/MS. *Chem. Eng. J.* **2010**, *157*, 373–378. [CrossRef]

56. Zhang, J.; Zhang, L.; Shi, Y.; Xu, G.; Zhang, E.; Wang, H.; Kong, Z.; Xi, J.; Ji, Z. Anatase TiO_2 nanosheets with coexposed {101} and {001} facets coupled with ultrathin SnS_2 nanosheets as a face-to-face n-p-n dual heterojunction photocatalyst for enhancing photocatalytic activity. *Appl. Surf. Sci.* **2017**, *420*, 839–848. [CrossRef]

57. Moustakas, N.G.; Kontos, A.G.; Likodimos, V.; Katsaros, F.; Boukos, N.; Tsoutsou, D.; Dimoulas, A.; Romanos, G.E.; Diony-siou, D.D.; Falaras, P. Inorganic–organic core–shell titania nanoparticles for efficient visible light activated photocatalysis. *Appl. Catal. B Environ.* **2013**, *130–131*, 14–24. [CrossRef]

58. Gao, J.; Sun, X.; Zheng, L.; He, G.; Wang, Y.; Li, Y.; Liu, Y.; Deng, J.; Liu, M.; Hu, J. 2D Z-scheme TiO_2/SnS_2 heterojunctions with enhanced visible-light photocatalytic performance for refractory contaminants and mechanistic insights. *New J. Chem.* **2021**, *45*, 16131–16142. [CrossRef]

59. Gao, J.; Hu, J.; Wang, Y.; Zheng, L.; He, G.; Deng, J.; Liu, M.; Li, Y.; Liu, Y.; Zhou, H. Fabrication of Z-scheme TiO_2/SnS_2/MoS_2 ternary heterojunction arrays for enhanced photocatalytic and photoelectrochemical performance under visible light. *J. Solid State Chem.* **2022**, *307*, 122737. [CrossRef]

60. Yan, X.; Ye, K.; Zhang, T.; Xue, C.; Zhang, D.; Ma, C.; Wei, J.; Yang, G. Formation of three-dimensionally ordered macroporous TiO_2@nanosheet SnS_2 heterojunctions for exceptional visible-light driven photocatalytic activity. *New J. Chem.* **2017**, *41*, 8482–8489. [CrossRef]

61. Wang, Z.; Chen, Y.; Zhang, L.; Cheng, B.; Yu, J.; Fan, J. Step-scheme CdS/TiO_2 nanocomposite hollow microsphere with enhanced photocatalytic CO_2 reduction activity. *J. Mater. Sci. Technol.* **2020**, *56*, 143–150. [CrossRef]

62. Dai, X.; Xie, M.L.; Meng, S.G.; Fu, X.L.; Chen, S.F. Coupled systems for selective oxidation of aromatic alcohols to aldehydes and reduction of nitrobenzene into aniline using CdS/g-C_3N_4 photocatalyst under visible light irradiation. *Appl. Catal. B Environ.* **2014**, *158*, 382–390. [CrossRef]

63. Luo, J.; Zhou, X.; Zhang, J.; Du, Z. Fabrication and characterization of Ag_2CO_3/SnS_2 composites with enhanced visible-light photocatalytic activity for the degradation of organic pollutants. *RSC Adv.* **2015**, *5*, 86705–86712. [CrossRef]

64. Kuldeep, A.R.; Dhabbe, R.S.; Garadkar, K.M. Development of g-C_3N_4-TiO_2 visible active hybrid photocatalyst for the photodegra-dation of methyl orange. *Res. Chem. Intermed.* **2021**, *47*, 5155–5174. [CrossRef]